

Characterization of Complex Dielectric Permittivity of Concrete by GPR Numerical Simulation and Spectral Analysis

Abstract:

In this paper, we present a numerical finite-difference time-domain (FDTD) simulation procedure developed to quantify the frequency-dependent ground penetrating radar (GPR) spectral responses occurring in four on-site scenarios involving concrete that is dry, half-saturated, saturated and chloride-contaminated. The responses are (1) numerically simulated by making use of the real and imaginary parts of complex permittivity derived from the GPR signal's two-way travel time and rebar reflection amplitude, respectively; then (2) characterized using Nyquist and Bode plots, and (3) compared to the wavelets obtained from authentic concrete specimens. The characterization shows good correspondence with the well-established Debye's models. Experimental validation shows that the simulated dispersion model is compatible with authentic concrete specimens when an optimal centre frequency is used. The method demonstrated in this paper can be used to convert GPR into a spectral analyser for predicting the on-site variability in material properties, the expected depth ranges of targets, and levels of attenuation and scattering before actual GPR survey.

Introduction

Ground penetrating radar (GPR) is a commonly used non-destructive testing (NDT) instrument for civil engineering purposes and its application on concrete has been widely studied, including its use for locating post-tension rebars, water leakage from pipes in walls and underground utility surveying. GPR antennas with a wide range of centre frequencies are available in the market to suit different surveying purposes; for example, ground investigations involving greater depth penetration require a GPR antenna with a lower centre frequency, whereas structural analysis in concrete makes use of high frequency GPR. Normally, the condition of surveyed materials/structures is assessed via C-scans, which are amplitude/energy plots of the surveyed area. In a complex subsurface environment, dispersion of EM waves may vary when the wide-band GPR signal encounters different materials. As signal attenuation is frequency-dependent, the study of dispersion at different frequencies helps with the understanding of GPR data collected from the surveying of different materials. Estimating the frequency-dependent permittivity spectrum is therefore important for the selection of the centre frequency and in the use of GPR results to predict the subsurface situation. This paper focuses on investigating the permittivity spectrum of concrete in wet and dry conditions using simulated GPR signals. This can be performed by using the Debye dispersion model with amplitude extraction and velocity analysis of GPR results from simulated data spanning a wide range of frequencies. Using this approach, a procedure for numerically simulating GPR signals as a basis for studying the complex dielectric permittivity of concrete or other materials is developed. This approach is also worth studying as a means of predicting the dielectric properties of other materials, including soils with a range of different conditions, such as those found surrounding underground utilities.

1.1 Principle of GPR

There are different types of GPR, but for civil engineering purposes impulse radar is typically used. Many GPR manufacturers develop impulse radars. For example, a GSSI 2 GHz impulse antenna is used in this study for concrete assessment, and other GSSI antennas with centre frequency 270 MHz, 400 MHz, 600 MHz and 900 MHz that are designed for surveying the underground, are all impulse antennas. Other manufacturers including IDS and Sensors and Software also offer impulse radars with a range of centre frequencies for road inspection and concrete condition assessment. An impulse radar consists of a transmitting (Tx) and receiving antenna (Rx), where the Tx emits an impulse signal into the subsurface and the Rx collects the refracted and reflected signals after they have propagated through different materials [10, 21]. The returned signals contain information about the reflection amplitude, phase change and propagating velocity, which can be used to derive the effective dielectric constant.

1.2 Dispersion of wave in materials

A dielectric medium (or an insulator) possesses a number of dielectric mechanisms (ionic, dipolar, atomic, electronic) contributing to the complex dielectric permittivity over a large frequency range [5, 7,20,25]. Electric charge carriers in the dielectric medium can be displaced by an incident electric field through experiencing a torque on the dipoles. This displacement is known as polarization $\epsilon''(\omega)$ which balances the electric field in such a way that the positive and negative charges move in opposite directions. The friction experienced by the dipolar orientation contributes to the losses in dielectric or permittivity values $\epsilon''(\omega)$. Both $\epsilon'(\omega)$ and $\epsilon''(\omega)$, as shown in Eq. (1) [5], are functions of angular frequency. At the microscopic level, several dielectric mechanisms have strong effects on the dielectric behaviour, in which dipole orientation governs the dielectric behaviour over the GPR's frequency range from MHz to GHz. The orientations of these dipolar moments are random when an electric field is absent because no polarization exists.

$$\epsilon = \epsilon' - j\epsilon'' \quad (1)$$

At low frequencies far below relaxation frequency, the slow E-field keeps the dipole in pace with the variations of the E-field (in-phase). Because the polarization is able to develop fully, the polarization storage $\epsilon'(\omega)$ and the absorption loss $\epsilon''(\omega)$ are independent of the frequency. As frequency increases to higher levels (including the microwave and also GPR region), the frictional and the inertial effects cause the polarization to lag behind the applied E-field such that a difference occurs. The response of the polarization becomes no longer instantaneous [13], which yields relatively small in-phase components between the input and response. It follows that the dipolar orientation does not fully contribute to the total polarization [20]. Hence, there is a constant drop of $\epsilon'(\omega)$ and subtle peak of $\epsilon''(\omega)$. This is known as dispersion of the dipolar/orientation polarization (see Figures in [14,15]) found at centre frequency 'f' or angular frequency ' ω ', and also the respective dielectric relaxation time ' τ ', shown in Eq. (2) and (3) [20, 23].

Beyond the relaxation frequency, both $\epsilon'(\omega)$ and $\epsilon''(\omega)$ drop as the applied electric field changes too fast and no longer influences the dipole rotation. Relaxation time measures the molecular (or dipolar) mobility of the material. It defines the time required for the dipoles to become oriented subject to an electric field or can be understood as the time required for the dipoles aligned in an electric field to return to 1/e of its random equilibrium value [1]. The movements of dipoles in liquid and solid states are limited by internal friction when an electric field is applied. When the applied E-field is turned off, the sequence is reversed to restore the random distribution with the same relaxation time constant.

The effect of the dipolar/orientation polarization was described by the seminal Debye's model [7] for pure materials and Cole and Cole's [5] models for composite materials. The existence of dielectric dispersion and relaxation time in a dielectric material result in an in-phase and an out-of-phase component in the polarization vector and is represented by the complex values of ϵ (i.e. $\epsilon = \epsilon'(\omega) - i\epsilon''(\omega)$). For a pure material that exhibits a single and well-defined polarization mechanism with a corresponding relaxation time (τ) (such as water), the effect of frequency dependence on dielectric permittivity is shown by the Debye's model [7]:

$$\epsilon'(\omega) = \epsilon_{\infty} + \frac{\epsilon_s - \epsilon_{\infty}}{1 + \omega^2\tau^2} \quad (2)$$

$$\epsilon''(\omega) = \omega\tau \left(\frac{\epsilon_s - \epsilon_{\infty}}{1 + \omega^2\tau^2} \right) \quad (3)$$

where ϵ_s and ϵ_{∞} are the static and infinite permittivity in the real part when angular frequency ($\omega = 2\pi f$) approaches 0 and infinity, respectively. $\epsilon'(\omega)$ and $\epsilon''(\omega)$ are the real and imaginary part of dielectric permittivity, respectively.

For other materials where well-defined polarization mechanisms do not exist, different polarization mechanisms and regions of dielectric dispersion render themselves as a spectrum of relaxation time as modelled by Cole and Cole [5], which added an exponent $(1-c)$ to the Debye's relaxation time in Eq. (2) and (3). 'c' is a distribution parameter that indicates the distribution of relaxation time in any composite material, where relaxation time is the reciprocal of the relaxation frequency, which is the peak of attenuation or a function of the frequency of the E-field.

Fig. 1 shows the graphical representation of complex dielectric permittivity of pure water [4], and a similar phenomenon can be observed in other materials. Information on dielectric relaxation is obtained by identifying the relaxation frequency and the points at which the angular frequency approaches zero and infinity. The dispersion zone is within the range of ϵ_s and ϵ_{∞} and the zone indicate the frequency range that exerts significant attenuation on GPR signals [10]. For example, the effect of water is significant at high frequencies (from 19 GHz as shown in Fig. 1).

Rhim and Buyukozturk [22] studied the EM properties of concrete in the microwave frequency range (0.1 to 20 GHz) by applying electrochemical methods with the use of an open-ended coaxial probe, which allowed the permittivity and conductivity to be explicitly identified. Concrete was assessed under different conditions (wet, saturated, air-dried and oven-dried) and the results showed that both the real and imaginary part of dielectric permittivity and electrical conductivity [22] are stable or have no significant change in the operating frequency range of GPR used for concrete assessment (0.1 to 4 GHz). The design of the coaxial cell contained a small sample holder with isotropic and homogeneous distribution of material properties, whereas GPR does not, and it is therefore worth investigating whether GPR can also be used to observe the capacitive behaviour of concrete.

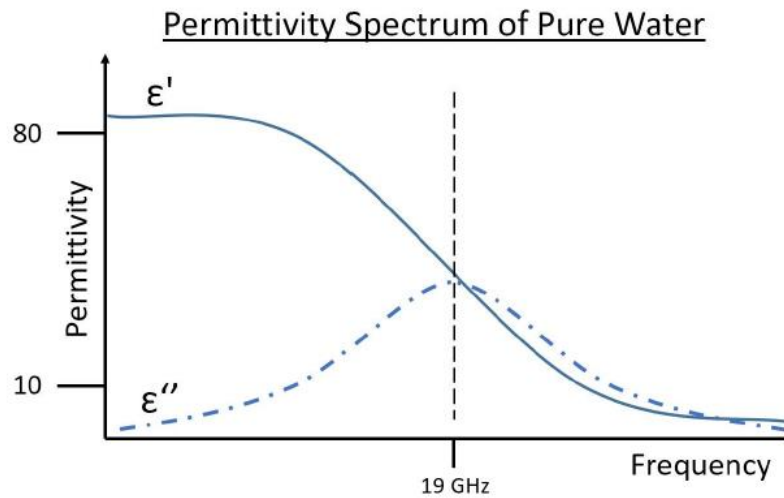


Fig. 1 Frequency-dependent permittivity spectrum of pure water displaying Debye relaxation mechanism

One main limitation with experimental measurements aimed at depicting the behaviour of complex dielectric permittivity using a coaxial probe is the huge number of samples and the sweep of the frequency spectrum involved. The use of a coaxial cell [24] solved part of the problem, but a huge sample size is unavoidable. We thus made use of a simulation tool, which offers an effective way to investigate the complex dielectric permittivity. Therefore, this paper aims to understand the practicality of using a coaxial probe to fill the gap between the measurement of EM properties and GPR signals by using numerical simulation.

1.3 Numerical simulation

In this work, the simulation software gprMax was used, which is an open-source piece of software that simulates EM wave propagation by using the finite-difference time-domain (FDTD) method, in order to numerically model GPR signals [27]. Users are able to build complex FDTD models of GPR using the text-based input file, with specification of all parameters for simulation such as model size, discretization, time window, and excitation, among other things. The FDTD method is a numerical solution of Maxwell's equations, which discretizes both the space and time continua [9] in differential form. This approach, which was initiated by Yee [11], is based on the discretization of the partial derivatives in Maxwell's equations using central differencing [8], and the resulting difference equations are then used iteratively to obtain solutions. When applied to the FDTD method, the discretization of spatial and time domains is required, where the steps required should be definitely specified due to the limited storage and processing speed. Hence the spatial and time domains are replaced by their discrete cells [8]. At each of the points within the discretized domain, a Yee cell is introduced. The cell proposed by Yee [11] is a building block of the discretized FDTD grid, as shown in Fig. 2. As a result, the 2D FDTD cell is obtained as a simplification of the 3D Yee cell.

The excitation of the FDTD model is achieved by introducing a source term in the electric $_eld$ at the location of the source. In order to deal with the boundary issues in modelling, gprMax uses perfectly matched layer (PML) absorbing condition boundaries (ABC) to absorb any waves that reach them,

thereby simulating an unbounded space. As suggested by the developers, the separation between the sources and targets, and the separation between free space and the sources should be at least 15 cells. This should be taken into account during the design stage of the simulation model. The FDTD modelled space is illustrated in Fig. 3.

The cell size should satisfy a rule-of-thumb in order to avoid numerical error during modelling. The rule is that the discretization step should be at least 10 times smaller than the wavelength. This requirement should be fulfilled while designing the model parameters.

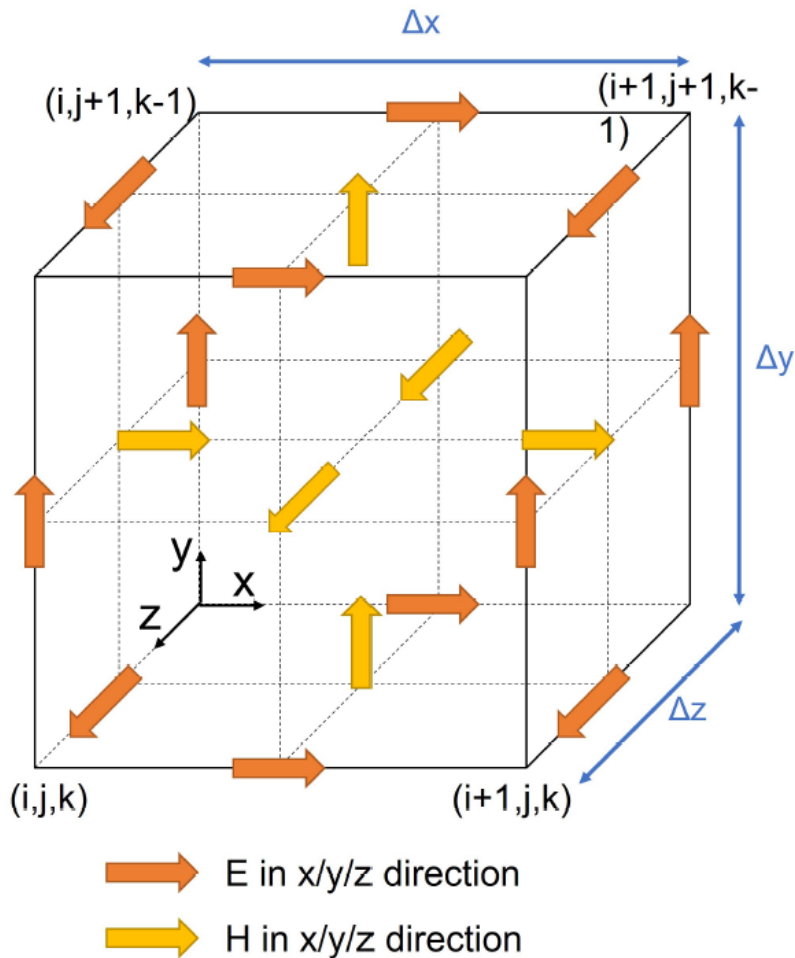
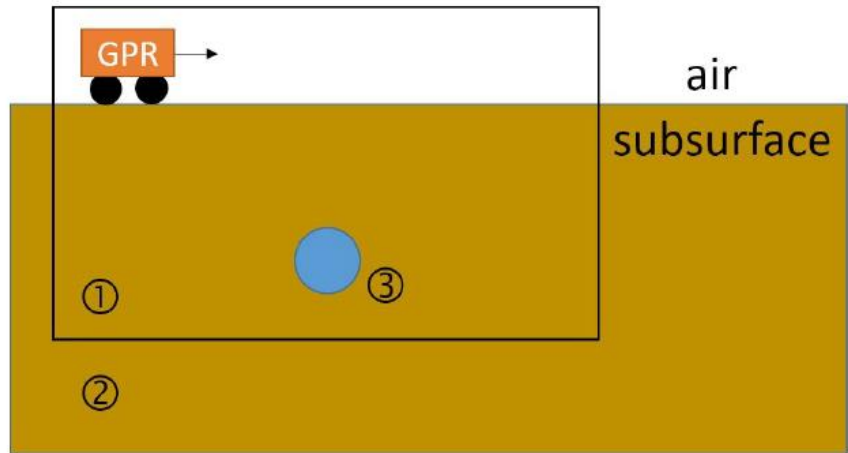


Fig. 2 A single FDTD Yee cell



- ① Inside the simulation model
- ② Outside the absorbing boundary
- ③ Target

Fig. 3 FDTD modelled space

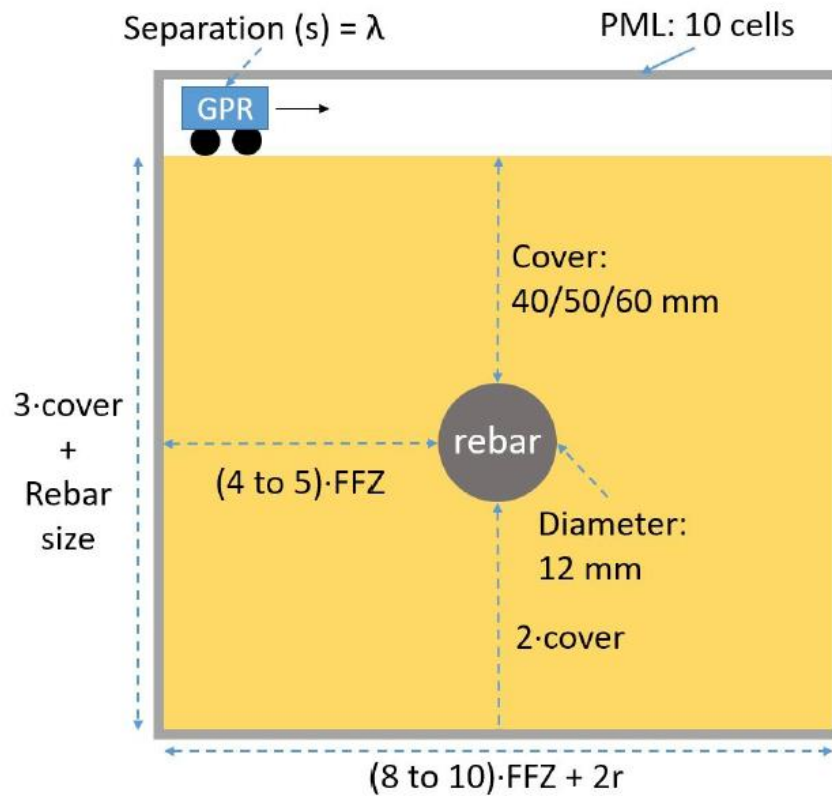


Fig. 4 Illustration of model design with respect to the FFZ

2 Research Method

2.1 Materials

2.1.1 Simulation

The model aims to simulate a block of concrete with a metallic circular object embedded in the centre (Fig. 4), and it is therefore important to define the dielectric properties (dielectric constant and electrical conductivity) of the material used in the model. The dielectric constant and electrical conductivity of concrete is estimated by the complex refractive index model (CRIM) (Eq. (4)) [10] and is assumed by ASTM STP 1276 [3,12] based on the conditions described, while the dielectric properties of the metallic object are pre-defined in the gprMax environment as a perfect electrical conductor (Tab. 1).

$$\varepsilon_{mix}^e = [(\phi S_w \sqrt{\varepsilon_w}) + ((1 - \phi) \sqrt{\varepsilon_m}) + (\phi (1 - S_w) \sqrt{\varepsilon_g})]^2 \quad (4)$$

where ε_{mix}^e is the effective permittivity of the mixture, ϕ is the porosity, S_w is the percentage of water saturation. ε_w , ε_g and ε_m are the permittivities of the water, gas and mixture phases, respectively.

Noted that [22] did not test chloride-intruded concrete, therefore the measurement of wet concrete is used as reference for Set C in this paper. This substitution is reasonable as the measured dielectric constant and conductivity of the wet concrete in [17] are significantly higher than the saturated concrete. A Ricker (or Mexican hat) wavelet (Fig. 5) is chosen. The frequency range is set with reference to the GPR plateau, which refers to the optimal frequency range for the application of GPR on different materials [2]. A Hertzian dipole is used as the source. gprMax offers several antenna models that imitate authentic commercial antennas. They cannot be used for this study because the antenna separation changes with the centre frequency. Therefore, the simulated wavelets are not modified by the antenna transfer function in this study, unlike a bowtie antenna model which is commonly found in commercial antennas for concrete inspection. Having said that, the frequency spectrum of an authentic impulse GPR signal in free space can be assessed easily. Users can refer to the actual centre frequency of the impulse signal and use the simulation results as references.

Table 1 Dielectric properties of concrete with different conditions for simulation

Scenario(s)	ϵ	σ (S/m)	Cover (mm)
D: dry	5.3	0.0001	40, 50, 60
HS: half-saturated	7.3	0.001	40, 50, 60
S: saturated	14	0.002	40, 50, 60
C: chloride-contaminated	14	0.01	40, 50, 60

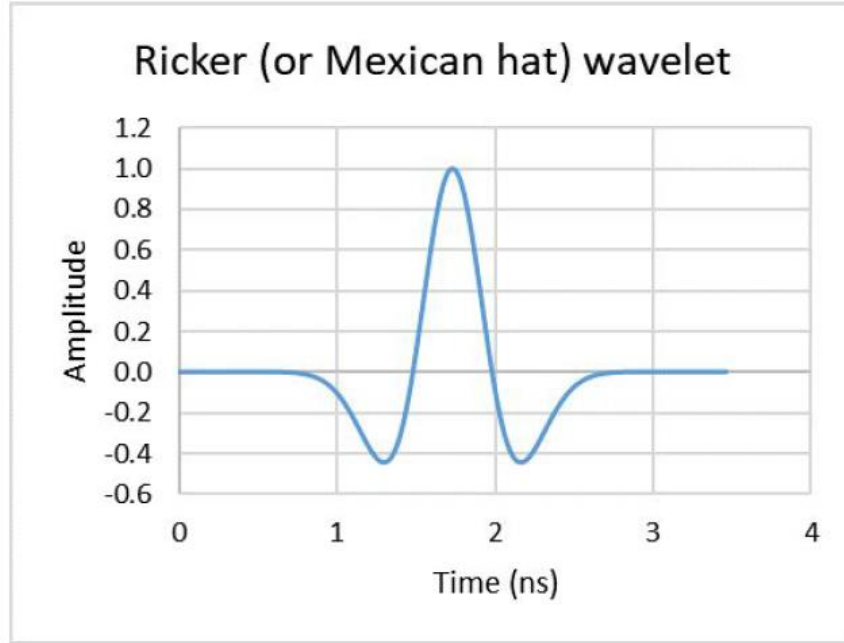


Fig. 5 A Ricker or Mexican hat waveform used in simulation as excitation wavelet

Some design parameters are controlled by the centre frequency, or in other words, the wavelength, and these are the model size, time window and antenna separation. The antenna separation is set as 1 wavelength with reference to the size of near_eld region of the antenna. The width and height of the model are controlled by the First Fresnel zone (FFZ) (Eq. (5)) [6] in order to obtain a hyperbolic reflection of the circular object with sufficient points to locate the apex for velocity analysis. This versatile method of determining model size also saves time when generating B-scans at higher frequencies with shorter wavelength, which results in a smaller model size than those produced at lower frequencies. Lastly, the size of time window is dependent upon the height of the model. The geometry of the resulting model is expressed in Fig. 4. It should be noted that the modelling of random inclusions of aggregate is not possible in gprMax, and therefore the different conditions being discussed in this paper consider concrete as a homogeneous medium with different levels of water and chloride saturation. Other configurations for the simulation and material properties are tabulated in Tab. 2 and the model was sufficiently well sampled and satisfied the numerical dispersion analysis in the gprMax environment [26].

$$FFZ = \sqrt{\frac{\lambda^2}{16} + \frac{\lambda D}{2}} \quad (5)$$

where λ is the wavelength (m), D is the cover depth (m).

Table 2 General configuration for gprMax input files

Spatial Discretization	2 mm in all directions
Centre Frequency	4/5/6/700 MHz to 3 GHz (depends on the concrete cover), with 100 MHz interval
Excitation Wavelet	Ricker wavelet
Step Size	2 mm
Source	Hertzian dipole

As shown above, the simulation model is very simple and contains only one rebar, unlike normal concrete structures where a rebar mesh is installed. A one-rebar model was designed because the simulation model is homogeneous, increasing the number of rebars does not provide reflected signals with different two-way travelling time (TTT) and amplitude. Unless the rebar spacing between the rebars are too narrow for the signals to resolve, this concern leads to the consideration of the First Fresnel zone (FFZ) of the GPR signal. As tabulated in Tab. 2, a low centre frequency (400 MHz) is used in simulation. It is reasonable to say that the FFZ of a signal with a low centre frequency is much greater than that with a high centre frequency. It is unrealistic to use a simulation concrete model with several rebars having a constant rebar spacing for a wide range of centre frequencies because the choice of antenna frequency is related to the location and depth of the target. A one-rebar design does not have the above issue.

Another reason for using a simple model is because it would be easier to transfer the same design rationale for other applications, e.g. underground utility surveying, in which a heterogeneous medium can be simulated in gprMax when lower frequencies are used. If this simple model work on concrete, this could also work for other cases. Due to the above reasons, a simple simulation model with one rebar is more appropriate for this study.

2.1.2 Authentic Concrete Specimens

Three concrete slabs (namely S2, F2 and G1, respectively) were used to validate the dispersion model (Fig. 6 and 7). They were selected by referring to the design parameters of the simulation model, which are the cover depth and EM properties (dielectric constant and conductivity).

Specimen S2 and F2 are twin specimens. S2 is prepared by 4% saline, where F2 is a normal concrete with the same structural design. The water-to-cement ratio is 0.65. The design compressive strength is 40 MPa. Ribbed steel bar of 20 mm diameter was used. The concrete cover is 40 mm (top-to-cover). Data were collected on Day 7 and 18 after concreting. Since the data were acquired during early-stage hydration, the condition of saturated (Set S) and chloride-intruded concrete (Set C) can be imitated.

Meanwhile, Specimen G1 is slightly different from S2 and F2. G1 is a normal concrete with 4 rebars of 12 mm diameter. The concrete cover is 40 mm (top-to-cover). The water-to-cement ratio is 0.57. The design compressive strength is 40 MPa. The condition of the specimen is intact and was at least 3 years old upon data collection. This air-dried specimen imitates either a half-saturated concrete (Set HS) or a dry concrete (Set D).

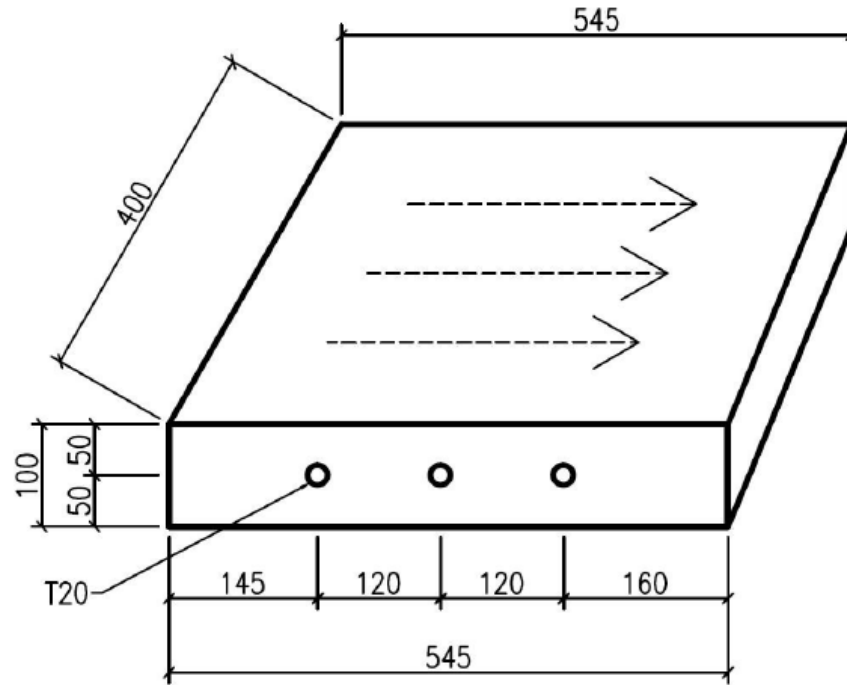


Fig. 6 Design of Specimen S2 and F2. The dashed arrows indicate the survey lines

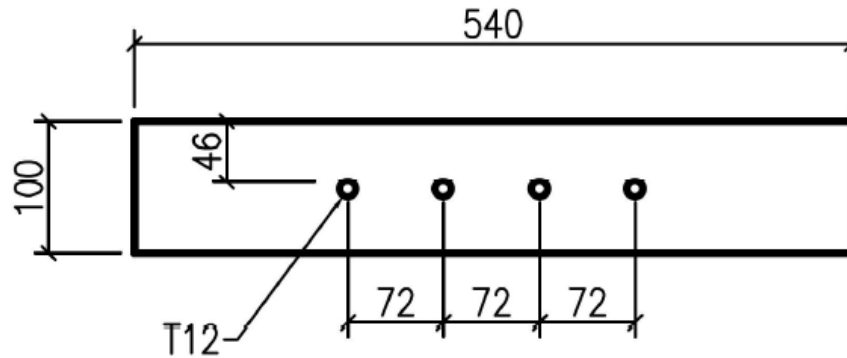


Fig. 7 Design of Specimen G1

As described in Section 2.1.1, the simulation model studies models with 40 mm cover, which is the same as the 3 concrete specimens. Although the rebar diameter of S2/F2 is 20 mm, not the same as the rebar used for simulation (12 mm), the focus of experimental validation is the dielectric constant, which is derived from the velocity. Therefore, the influence of concrete cover is primary, hence, the results of experimental validation can be compared to those obtained from numerical simulation.

Two sets of GPR systems, the Sensors & Software PulseEKKO Pro with a 1000 MHz antenna and the GSSI SIR 4000 with a 2000 MHz antenna, were employed. The experiments were conducted in a controlled environment in the laboratory.

2.2 Post-processing

2.2.1 Simulation

Fig. 8 shows the work ow of data extraction for generating $\epsilon'_$ and ϵ'' as a function of frequency. A series of B-scans covering the frequency range from 400 MHz to 3 GHz produced by simulation is used and the simulated B-scans do not require post-processing as in real GPR data because they are noise-free and therefore ready for data analysis. Amplitude extraction [28] and velocity estimation are performed to determine signal attenuation at varying frequencies and the propagation velocity, respectively, which are then used to plot the frequency-dependent dielectric permittivity.

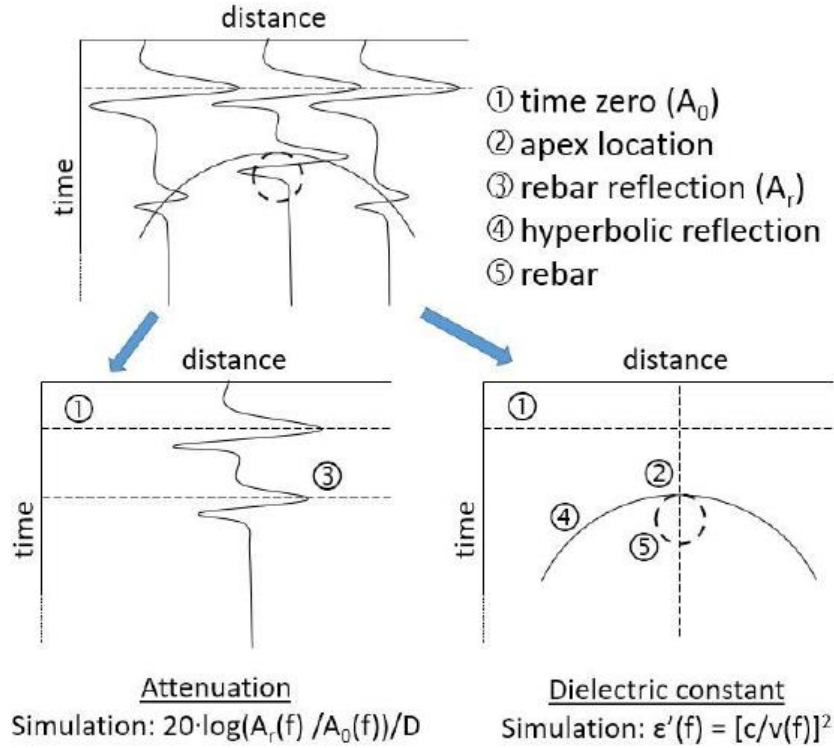


Fig. 8 Illustration of the flow for data extraction of ϵ' and ϵ'' in simulation

Attenuation is described by the ratio of rebar reflection amplitude (A) and the maximum measurable amplitude of a 16-bit data storage system (A_0) in log scale (Eq. (6)), whereas the propagation velocity is calculated by converting the two-way travel time (TTT) into the real part of complex permittivity (ϵ'') across the whole frequency range (Eq. (7)).

$$\text{Attenuation of amplitude (dB/m)} = 20 \cdot \log(A/A_0)/D \quad (6)$$

$$\epsilon' = (ct/2D)^2 \quad (7)$$

$$v = 2D/t \quad (8)$$

where t is the two-way travel time (ns), c is the speed of light in vacuum (m/ns), and D is the cover depth (m).

Fig. 9 shows the illustration of the resulting plots of attenuation and $\epsilon'_$. The relaxation time (τ) of concrete in Eq. (2) and (3) is defined as the reciprocal of the peak angular frequency (f_{peak}) observed in the plot of attenuation, while the static frequency (ϵ_{s}) and infinite frequency ($\epsilon_{\text{infinity}}$)

of relative permittivity can be identified from the flattened plateau at either end of the plot of ϵ'' . The static and infinite frequencies are then substituted into the Debye's model to plot the curve of the imaginary part of complex permittivity, and then combining the 2 parts results in a Debye's dispersion model.

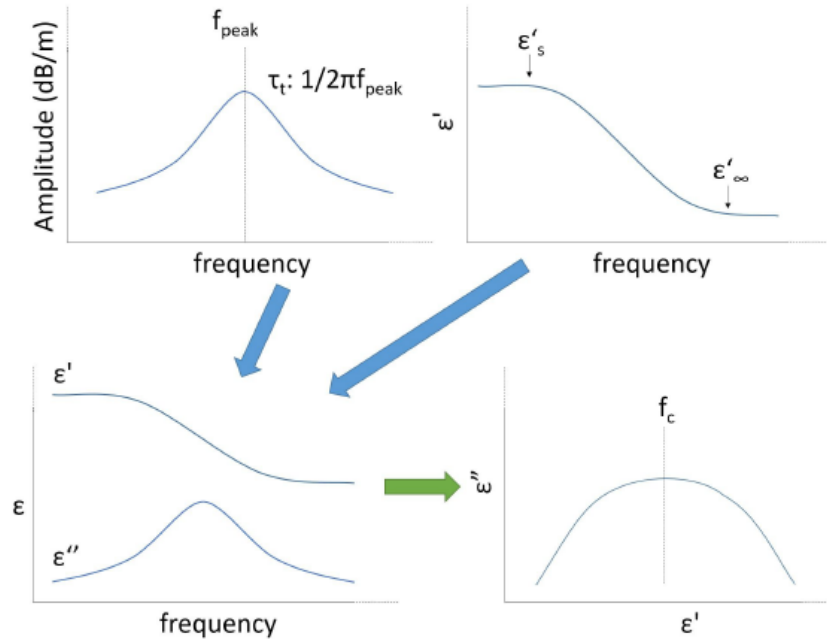


Fig. 9 Dispersion (top), Bode (bottom left) and Nyquist plot (bottom right) in simulation

Amplitude is normalized by using Eq. (6) and is then plotted against frequency, whereupon a small hump should be observed that indicates the location of f_{peak} . The calculated value of ϵ'' for the lowest frequency that exceeds the frequency range for simulation is extrapolated to 0 Hz with reference to the value obtained by [22]. As the effective dielectric constant computed from simulated data is affected by the near-eld effect, a standard value or reference value is required at 0 Hz, whereas $\epsilon_{infinity}$ is the ϵ'' value at 3 GHz (by extrapolation), while ϵ' is expected to be stable in high frequency range. The f_{peak} , ϵ'_s and $\epsilon_{infinity}$ are then substituted into Eq. (2) and (3) to produce the Debye's permittivity spectrum. Wavelet transform (WT) (Eq. (9) and (10) [16]) is applied to obtain the WT frequency spectra of the reflected wavelets, such that the effect of different concrete scenarios (different dielectric constant and conductivity) can be observed in the time-frequency domain.

$$\psi_0(t) = \frac{1}{\sqrt[4]{\sigma^2\pi}} \exp\left(-\frac{t^2}{2\sigma^2} + j\omega_0 t\right), \text{ where } \omega_0 = 1.5\pi \quad (9)$$

$$\text{Integral continuous form } WT_{u,a} = \langle s, \psi_{u,a} \rangle = \int_{-\infty}^{\infty} s(t)\psi_{u,a}^*(t)dt \quad (10)$$

where mother wavelet $\psi_{u,a} = \frac{1}{\sqrt{a}}\psi\left(\frac{t-u}{a}\right)$

$\psi_{u,a}^*$ is known as a mother wavelet or in this case we used a complex-valued Morlet wavelet, or Gabor wavelet, u is the shift factor and a is the scale factor of the wavelet. $\psi_{u,a}^*$ is the complex conjugate of $\psi_{u,a}$.

2.2.2 Authentic Concrete Specimens

DC shift removal and Butterworth frequency filtering (band-pass: 400-4000 MHz) were applied for post-processing. The WT frequency spectra of the reflected wavelets and the associated peak frequency response of the rebar was obtained by using wavelet transform (Eq. (9) and (10) [16]). To better represent the propagation of GPR waves in reality, the multi-triangulated ray-path method (Eq. (11)) was used for velocity estimation [29]. This method considers the concrete cover, the radius of rebar and the antenna separation. This approach is more realistic and accurate than using the two-way travel time (TTT) for velocity estimation.

$$v_i = \frac{1}{t_i} * \left\{ \sqrt{\left[(D_0 + r) - \frac{(D_0 + r)r}{\sqrt{(D_0 + r)^2 + (x * \sin\theta)^2}} \right]^2 + \left[\left((x * \sin\theta) - \frac{r \times (x * \sin\theta)}{\sqrt{(D_0 + r)^2 + (x * \sin\theta)^2}} \right) - S \right]^2} \right. \\ \left. + \sqrt{\left[(D_0 + r) - \frac{(D_0 + r)r}{\sqrt{(D_0 + r)^2 + (x * \sin\theta)^2}} \right]^2 + \left[\left((x * \sin\theta) - \frac{r \times (x * \sin\theta)}{\sqrt{(D_0 + r)^2 + (x * \sin\theta)^2}} \right) + S \right]^2} \right\} \quad (11)$$

where v_i , t_i are the estimated velocity and the two-way travel time measured by the GPR when the antenna is at position x_i , respectively. D_0 is the known cover depth of the rebar, r is the radius and S is half of the antenna separation, and θ is the included angle between the direction of GPR traverse and the alignment of the rebar.

3 Findings and Discussion

Fig. 10 summarizes the data extracted from the simulated B-scans and there are 2 notable observations: 1) a hump appears in every attenuation set at a different frequency, and 2) the effective dielectric constant becomes abnormally high in the frequency range lower than that frequency. This frequency is also known as the characteristic frequency (f_c) [18], which implies that the EM waves cannot propagate when the frequency of the GPR signal is lower than f_c as, which is when energy dissipation becomes the dominant mechanism. In practice, this means that for any given material conditions, a GPR with a centre frequency smaller than the f_c must not be used.

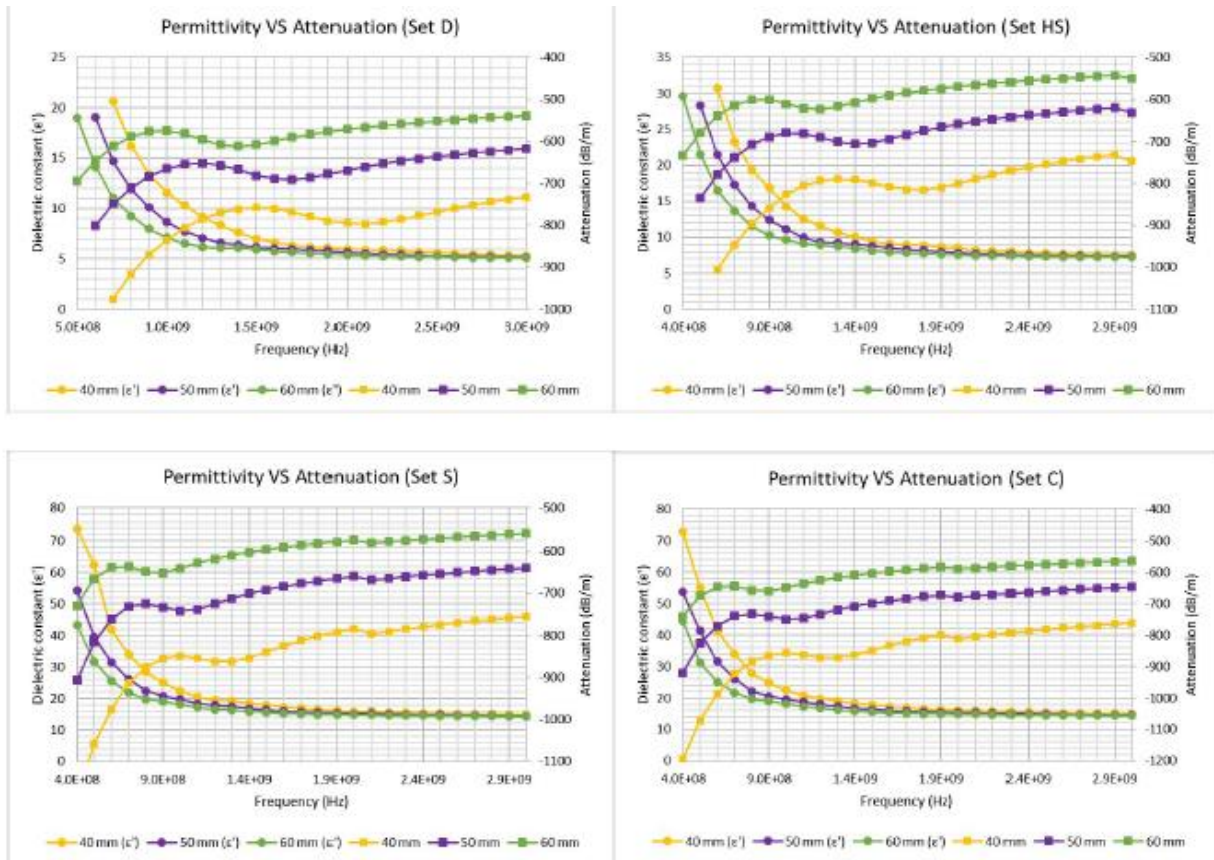


Fig. 10 Simulated effective dielectric constant VS attenuation (D: dry, HS: half-saturated, S: saturated, C: chloride-contaminated)

3.1 Effects on concrete conditions simulated in the four scenarios

The resulting permittivity spectra of different concrete conditions are presented in Bode and Nyquist format in Fig. 11 and 12, respectively.

The Bode format explicitly shows the change of both components against frequency, where the real components are higher at the high frequency end in all conditions, and the scale of difference of the imaginary component is significantly smaller in Set D (dry concrete), indicating that the attenuation can be considered negligible. As described by Persico [19], if the real component of permittivity is greater than the imaginary part by an order of magnitude, the material is considered low-lossy. This result was also found in the other 3 conditions, although the scale of difference of the imaginary part is larger than that in Set D, but it can be concluded that the concrete in all these 4 conditions can be characterized as low-lossy. In addition, the effect of conductivity is illustrated by Set S (saturated concrete) and Set C (chloride-contaminated) in Bode representation. From Fig. 11c & d, we can see that the imaginary part in Set C (chloride-contaminated) is twice as large as that in Set S, showing that attenuation is twice as strong at the same frequency, but this difference is less obvious in the real part as the overall change is rather insignificant.

The Nyquist representation of the permittivity reveals more about the concrete. In all 4 conditions, extrapolated values outside of the measurable frequency region (simulation stops at 3 GHz) are expressed

as hollow circles and checked lines. Highly depressed semi-circles can be observed, and the extent of their depression is related to the dielectric behaviour of the material: the higher the degree of depression, the smaller the dielectric. Concrete as a mainly solid composite material has a smaller dielectric, and therefore the depression of the semi-circle is high. We can also see in Tab. 3 that the extent of depression in different conditions has a relationship with the designed dielectric constant of concrete, where the shape is less depressed as the dielectric constant increases, or to put it another way, as the capacitance decreases.

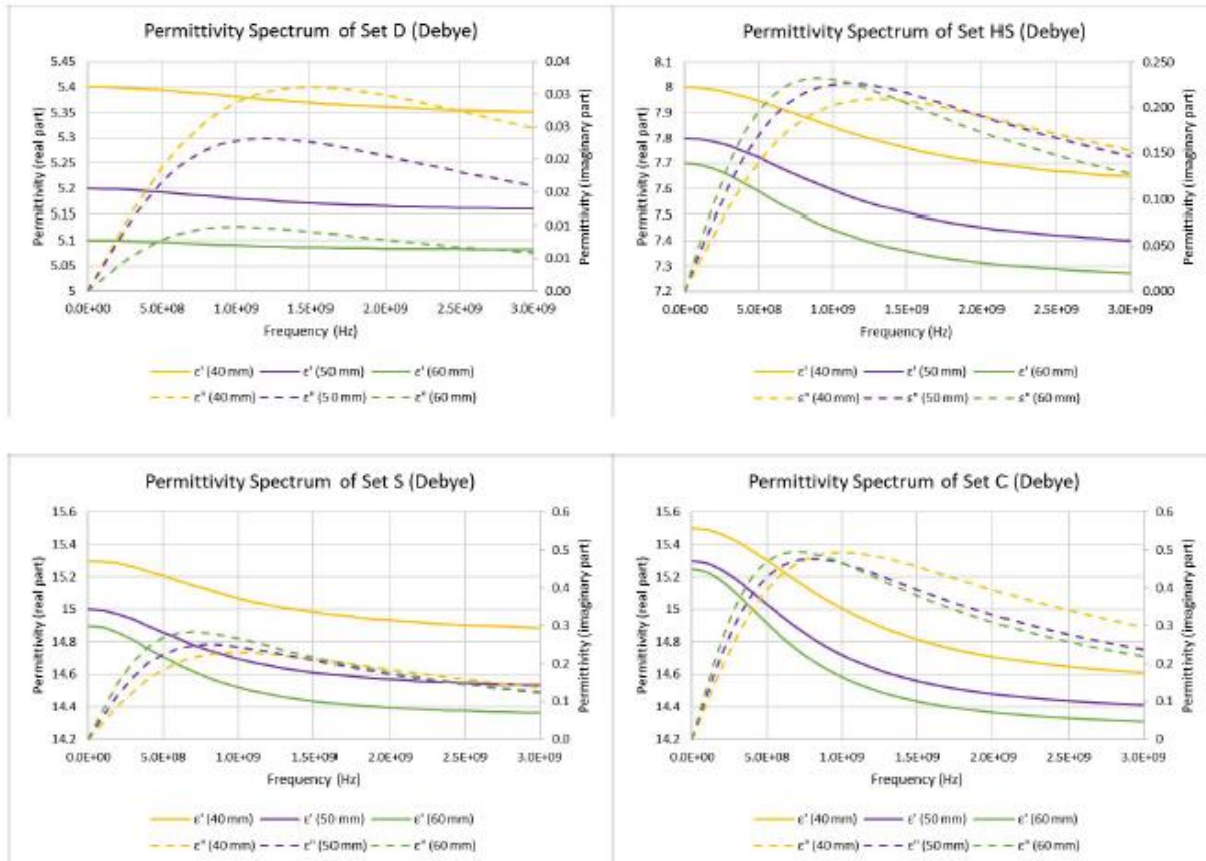


Fig. 11 Simulated permittivity spectrum of concrete in Bode format (D: dry, HS: half-saturated, S: saturated, C: chloride-contaminated)

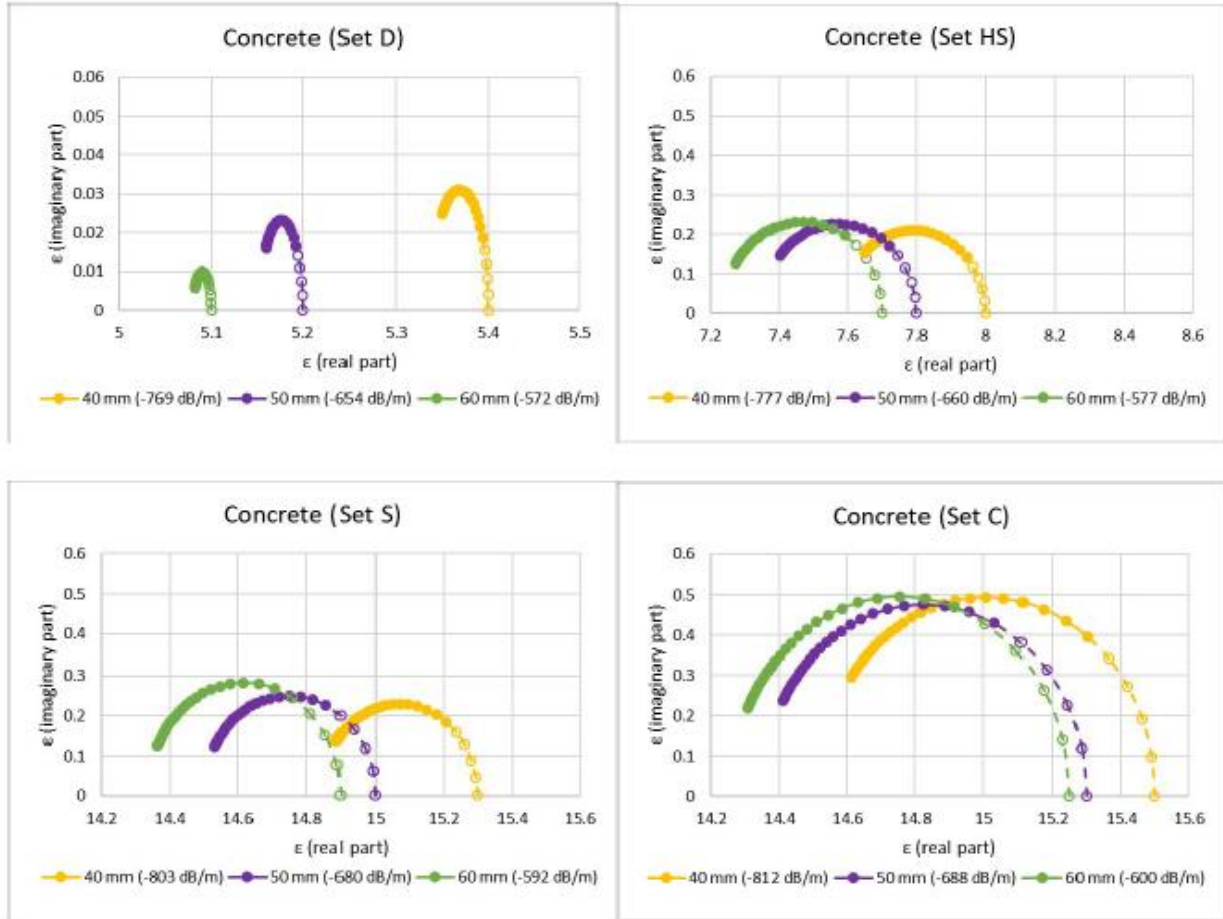


Fig. 12 Simulated permittivity spectrum of concrete in Nyquist format (D: dry, HS: half-saturated, S: saturated, C: chloride-contaminated)

Table 3 Extent of depression of semi-circle (width ratio of ϵ'' : ϵ')

Cover	D ^a (ϵ' : 5.3)	HS ^a (ϵ' : 7.3)	S ^a (ϵ' : 14)	C ^a (ϵ' : 14)
40 mm	0.50 (-792 dB/m)	0.43 (-777 dB/m)	0.33 (-803 dB/m)	0.33 (-812 dB/m)
50 mm	0.40 (-654 dB/m)	0.37 (-660 dB/m)	0.27 (-680 dB/m)	0.27 (-688 dB/m)
60 mm	0.33 (-572 dB/m)	0.30 (-577 dB/m)	0.23 (-592 dB/m)	0.23 (-600 dB/m)

^a D: dry, HS: half-saturated, S: saturated, C: chloride-contaminated

In conclusion, these 2 formats of permittivity spectra show that the dielectric behaviour of concrete generally complies with the Debye model, and the dielectric behaviour is more stable in concrete at higher frequencies (up to 3 GHz). The summary of f_c results is tabulated in Tab. 4 and it can be seen that most of the f_c values fall within the frequency response range for normal or chloride-contaminated concrete when a 2 GHz impulse antenna is used. According to the permittivity relaxation phenomenon [10, 6, 25], the dipole moment of the molecules in the material becomes increasingly vigorous when the alternating frequency of the applied electric field approaches f_c , which leads to an increase in the imaginary component as the energy initially stored in the molecules is lost as heat when the molecules rotate;

meanwhile, since there is less energy being stored in the molecules, the real component decreases. After reaching f_c , the molecules can no longer react to or rotate with the applied electric field, and both components therefore decrease and stabilize as the frequency increases further. With reference to this mechanism, we can conclude that the signal attenuation is generally stable in the context of amplitude analysis for normal or chloride-contaminated concrete.

Table 4 Characteristic frequency of concrete in GHz

Cover	D ^a (ϵ' : 5.3)	HS ^a (ϵ' : 7.3)	S ^a (ϵ' : 14)	C ^a (ϵ' : 14)
40 mm	1.5 (-792 dB/m)	1.3 (-777 dB/m)	1.0 (-803 dB/m)	1.0 (-812 dB/m)
50 mm	1.2 (-654 dB/m)	1.1 (-660 dB/m)	0.8 (-680 dB/m)	0.8 (-688 dB/m)
60 mm	1.0 (-572 dB/m)	0.9 (-577 dB/m)	0.7 (-592 dB/m)	0.7 (-600 dB/m)

^a D: dry, HS: half-saturated, S: saturated, C: chloride-contaminated

As shown in Fig. 13, depth-dependency is insignificant; however, the imaginary component is generally higher in the lower frequency region (> 1.5 GHz) and lower in the higher frequency region as the concrete cover increases. This behaviour is likely to be due to the fact that concrete is a low-lossy material, and therefore the overall permittivity behaviour is stable across the frequency range from 0 to 3 GHz regardless of the depth.

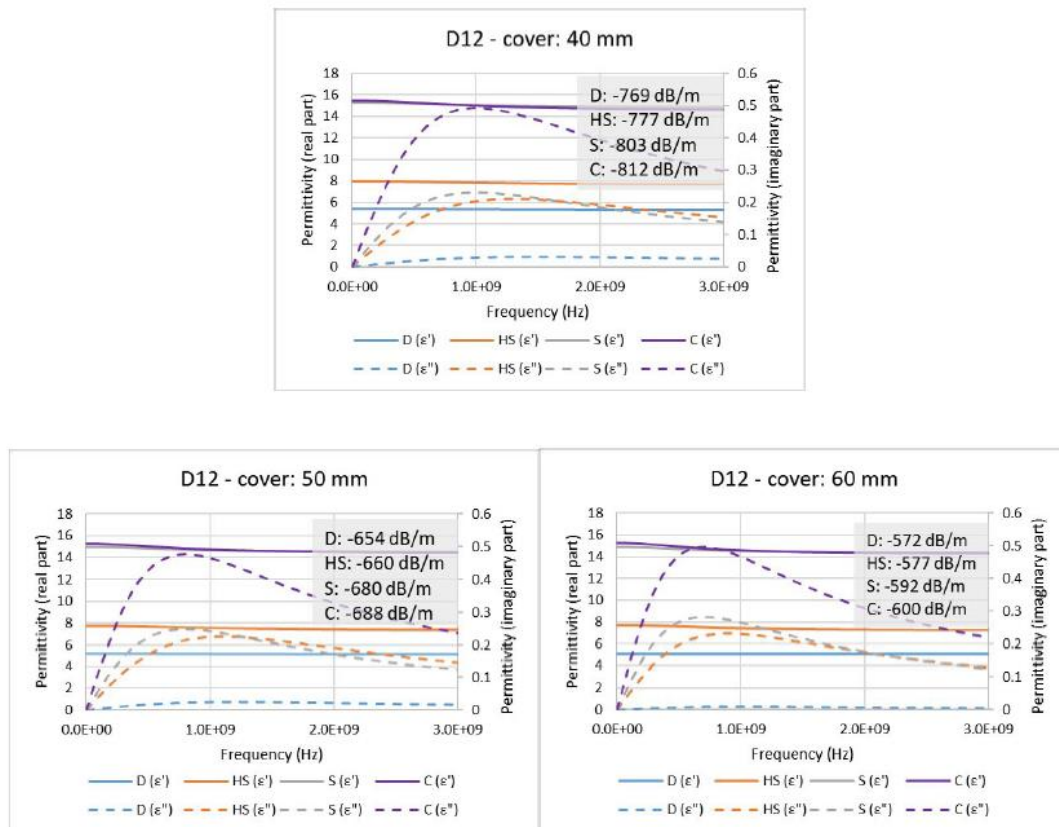


Fig. 13 Relationship of simulated dielectric permittivity with concrete cover (D: dry, HS: half-saturated, S: saturated, C: chloride-contaminated)

To sum up, the above numerical results match with the experimental results reported by Rhim and Buyukozturk [22], in that both sets of results show that the dielectric properties of concrete are rather stable in the GPR operating frequency range for concrete inspection (up to 3 GHz), and the imaginary component has a close relationship with the electrical conductivity, which is not explicitly depicted in the real part. We can conclude that it is practical to use numerical GPR data to study the dielectric properties of concrete under different conditions.

3.2 Experimental Validation

Fig. 14 shows the B-scans of the three specimens for experimental validation. The difference between the center frequency of the antenna and the condition of concrete can be observed. In comparison, it is clearly shown that the superposition of the hyperbolic reflection of rebars in G1 and the direct wave is more severe than that in S2 and F2 when the 1 GHz antenna is used. This is because the dielectric constant of G1 as a rather dry and intact concrete is considerably lower, hence, the signal travels faster in G1. The superposition is also due to the difference in wavelength between the signals emitted from the 2 antennas. The wavelength of an impulse signal with center frequency at 1 GHz is wider than a 2 GHz signal. In addition, as the 2 rebars in the middle of G1 cannot be clearly examined, only the leftmost and rightmost rebar of G1 are studied in this paper.

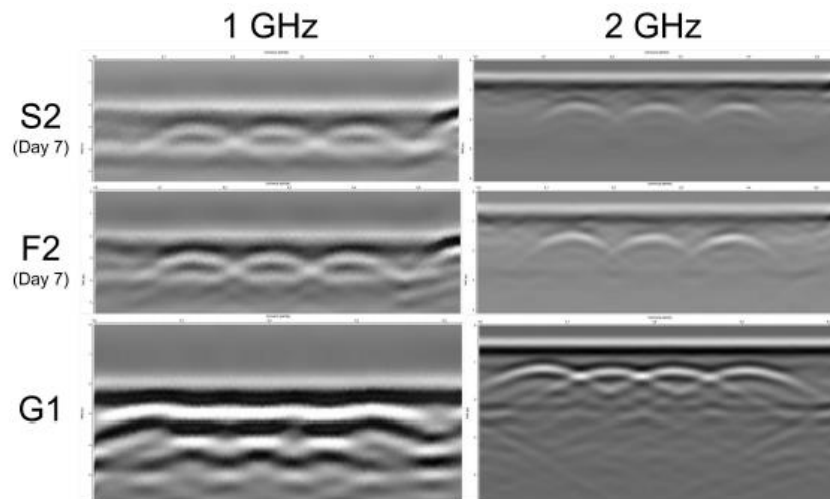


Fig. 14 B-scans of the three specimens for experimental validation

To compare with the experiment results, Fig. 15 shows the modified effective dielectric constant of the simulated GPR data derived from the velocity estimated by the multi-triangulated ray-path method (Eq. (11)). The change of epsilon in the region of lower frequency is opposite to Fig. 10 and 11. Such difference is highly influenced by the antenna separation. Eq. (11) shows that the estimated velocity is proportional to the antenna separation. Therefore, when the concrete cover (D) and the radius of rebar (r) are fixed, the increase in antenna separation results in a faster velocity. The antenna separation of the 1 GHz antenna (15 cm) is greater than the 2 GHz antenna (4 cm).

Another non-fixed variable is the travelling time. The travelling time of the 1 GHz data is greater than the 2 GHz data in general, but the difference is rather small when compared to the difference between the antenna separation (S). As a result, the effect of antenna separation is dominant. The estimated velocity is summarized in Tab. 5. It is clear that the estimated velocity associated with the 1 GHz antenna is

significantly higher. They are also abnormally high when compared to the normal range of GPR velocity in concrete (0.095-0.134 m/ns [3]). In fact, the rebars are all located within the radiative near field of the 2 antennas. However, the boundary of the near field of the 1 GHz antenna is considerably further away from the rebars when compared to the 2 GHz antenna. According to the characteristics of near field, the angular field distribution becomes more in phase as the signal approaches the boundary of near field, meaning that the relationship between the E and H-field gradually becomes less complex. Measurement is therefore more reliable outside the near field.

Another parameter of concern is the average dielectric constant derived from the estimated velocity. The ϵ_0 derived from the 1 GHz data is abnormally low (normal range: 5-10 [3]). This is because the estimated velocity is abnormally high. Again, the result of the 1 GHz antenna is not reliable because of the influence of near field. Finally, the ϵ' derived from experiment result is compared to the simulated dispersion model (Fig. 15) and the design model parameter (Tab. 1). The % difference at 1 GHz is strikingly high and not sensible. In contrast, the % difference at 2 GHz is much smaller, especially the % difference with the dispersion model (Fig. 15). This observation shows that, when an optimal center frequency is chosen for GPR measurement, in addition to an accurate velocity estimation, the ϵ' provided by the dispersion model is rather reliable. On top of that, the model parameters should be adjusted for different host media, such that the resultant dispersion model could be more realistic and case specific.

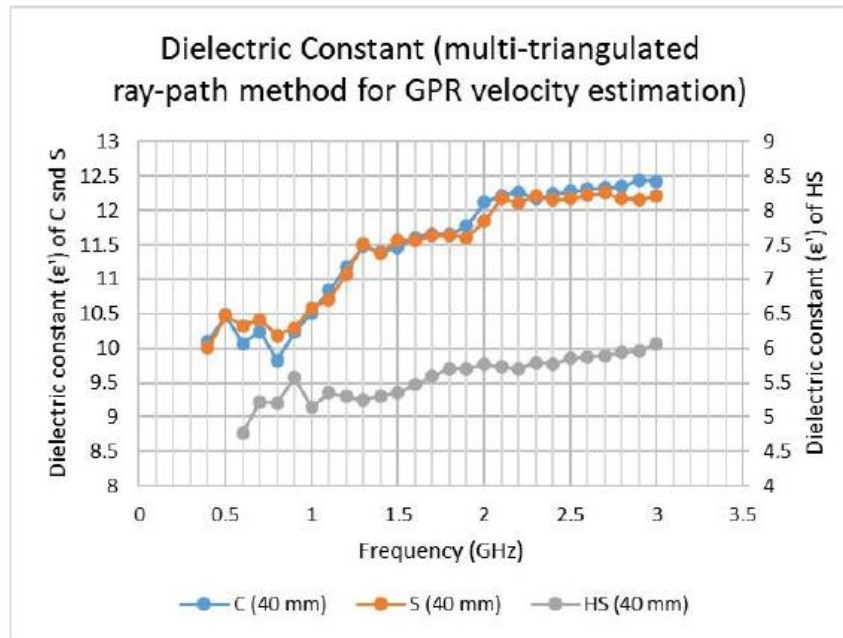


Fig. 15 Effective dielectric constant of Set S, C and HS with concrete at 40 mm derived from GPR velocity estimated by the multi-triangulated ray-path method

Table 5 Summary of experimental validation

Specimen	Peak frequency response from WT (GHz)	Estimated velocity (m/ns) ^a	Boundary of radiative near field (m) ^{b,c}	Average dielectric constant	% difference with the dispersion model ^d	% difference with the design model parameter ^e
S2 (Day 7)	1	0.145	0.145	4.29	59.2%	69.4%
S2 (Day 18)	1	0.147	0.147	4.16	60.5%	70.3%
F2 (Day 7)	1	0.152	0.152	3.90	63.2%	72.2%
F2 (Day 18)	1	0.157	0.157	3.63	65.7%	74.1%
G1	1	0.182	0.182	2.72	47.1%	62.8%
S2 (Day 7)	1.8	0.092	0.051	10.57	9.3%	24.5%
S2 (Day 18)	2	0.094	0.047	10.25	15.4%	26.8%
F2 (Day 7)	2	0.096	0.048	9.78	17.5%	30.2%
F2 (Day 18)	2	0.097	0.049	9.54	19.5%	31.8%
G1	2.5	0.121	0.048	6.15	5.1%	15.7%

^a uses the multi-triangulated ray-path method with known depth, radius of rebar and antenna separation

^b the boundary of radiative near field is defined as 1 wavelength

^c the concrete cover is 40 mm to the surface of rebar

^d S2 (Day 7 and 18) refers to Set C, F2 (Day 7 and 18) refers to Set S, and G1 refers to Set HS in Fig. 15

^e as defined in Table 1

3.3 Comparison of WT Frequency Spectra

Fig. 16 and Fig. 17 show the comparison of frequency spectra between the simulated data and experimental validation. Results show that the amplitude of authentic GPR signals are significantly higher than the simulated signals. The peaks of the frequency spectra of the 1 GHz signals are very close to each other. The differences between the amplitude among different concrete scenarios are also consistent between the simulated data and experimental validation. As for the 2 GHz signals, it can be seen that peaks of frequency spectra shift to the lower end with increasing dielectric constant and electrical conductivity, this is unlike the observation in the 1 GHz signals (Fig. 16). Another observation is that the frequency peaks of the experimental validation sets are also away from the frequency peaks of the simulated signals towards the lower end. It shows that attenuation is in fact greater in authentic concrete specimens at higher frequency, because more high frequency components dissipate while travelling in authentic concrete specimens due to scattering attenuation and the Maxwell-Wagner effect, where dipole moment occurs when the signals encounter chloride ions [10]. To sum up, the results indicate that the simulated Ricker wavelets and the wavelets obtained from authentic concrete specimens can match in general.

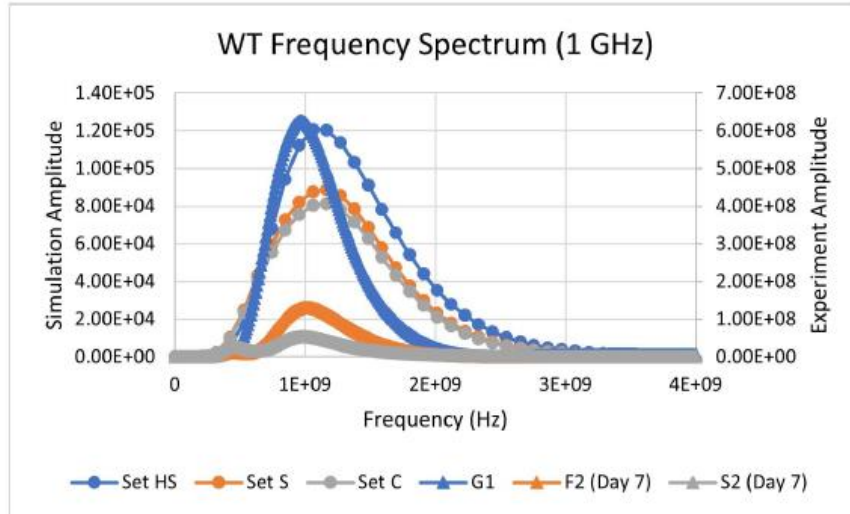


Fig. 16 Frequency Spectrum of Simulated data and experimental validation at 1 GHz. Simulation: Set HS, S and C. Experimental Validation: G1, F2 (Day 7) and S2 (Day 7).

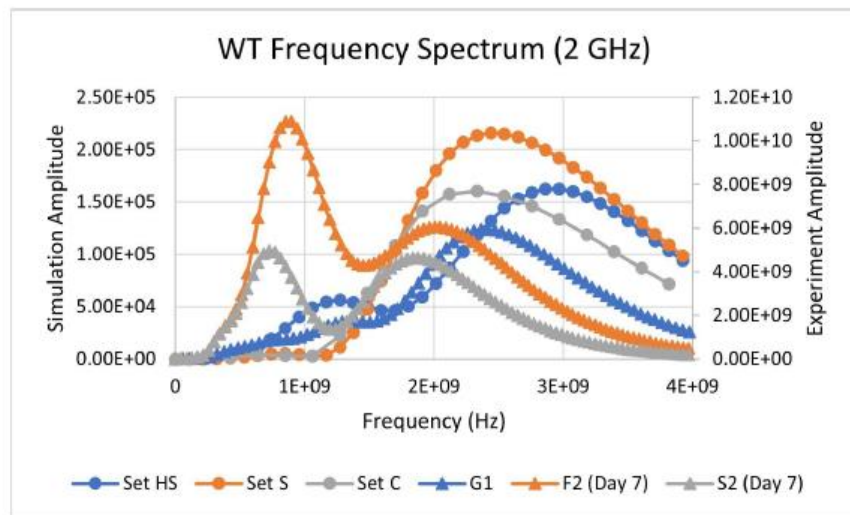


Fig. 17 Frequency Spectrum of Simulated data and experimental validation at 2 GHz. Simulation: Set HS, S and C. Experimental Validation: G1, F2 (Day 7) and S2 (Day 7).

In conclusion, neither the dispersion model in Fig. 10 nor Fig. 15 provides an accurate dielectric constant in the lower frequency range, because only the estimated dielectric constant in the higher frequency region provides good reference. The derived dielectric constant is reliable within the GPR plateau. Such result is produced because antenna with lower center frequency is not suitable for concrete condition assessment. The above findings show that it is essential to choose an optimal frequency that considers the relationship between the antenna design and the target object. In this case, the 1 GHz antenna is not suitable for all scenarios studied in this paper because all the cover depths are less than half of the near field. The same logic is applicable to underground utility (UU) survey as well. For example, an impulse radar with center frequency at 600 MHz is a suitable choice for UU survey because the pipes are usually located in the far field of the antenna.

4 Conclusion

This paper presented a numerical method for studying the dispersion of GPR signals in concrete under different conditions. The simulated wavelets were characterized and compared to measurements obtained from authentic concrete specimens in the time domain and time-frequency domain. The derived permittivity spectra display a GPR plateau as the excitation frequency of the wavelet increases. It aligns with the Debye's formulation and shows the optimal frequency range for concrete assessment. The comparison of the WT frequency spectra shows that the behaviors of the signals between simulation and measurements are similar, except for the fact that scattering attenuation is not as substantial as it is in authentic concrete specimens, which result in a higher peak frequency response than those obtained from measurements. Despite of this discrepancy, the GPR plateau provides reference for GPR users to choose a suitable centre frequency for the task.

In summary, the results show that using numerical simulation to study dispersion of EM waves in concrete is feasible, and this method is able to remove the need to prepare numerous samples for studying the dielectric properties of material by coaxial probe. The findings could be further utilized in the simulation of concrete for different purposes by including dispersive or non-dispersive material within Debye's formulation. By predicting the GPR responses to parameters of interest such as cover depth to the object, depth range dispersion and wave propagation velocity in media, surveys on concrete and the underground environment could be predicted with the aid of simulated permittivity spectra before an actual field survey is carried out.

References

1. Agilent: Basics of Measuring the Dielectric Properties of Materials, Application Notes. Agilent (2005)
2. Annan, A.P.: Ground Penetrating Radar Applications, Principles, Procedures. Sensors and Software, Mississauga, Canada (2004)
3. ASTM: ASTM D6432-11: Standard Guide for Using the Surface Ground Penetrating Radar Method for Subsurface Investigation. ASTM (2011)
4. Cassidy, N.J.: Ground Penetrating Radar: Theory and Applications, book section 2, pp. 41{72. Elsevier Science, Amsterdam, the Netherlands (2009)
5. Cole, K.S., Cole, R.H.: Dispersion and absorption in dielectrics i. alternating current characteristics. The Journal of chemical physics 9(4), 341{351 (1941)
6. Daniels, D.J.: Ground penetrating radar, second edn. London : Institution of Electrical Engineers, London (2004)
7. Debye, P.J.W.: Polar molecules. Dover Publications, New York (1960)
8. Giannopoulos, A.: The Investigation of Transmission-Line Matrix and Finite-Difference Time-Domain Methods for the Forward Problem of Ground Probing Radar. Thesis, University of York (1997)
9. Giannopoulos, A.: Modelling ground penetrating radar by gprmax. Construction and Building Materials 19(10), 755{762 (2005). DOI

<https://doi.org/10.1016/j.conbuildmat.2005.06.007>

10. Jol, H.M.: Ground Penetrating Radar: Theory and Applications. Oxford: Elsevier, Amsterdam, the Netherlands (2009)
11. Kane, Y.: Numerical solution of initial boundary value problems involving maxwell's equations in isotropic media. IEEE Transactions on Antennas and Propagation 14(3), 302{307 (1966). DOI <https://doi.org/10.1109/TAP.1966.1138693>
12. Klingho_er, O.: Techniques to assess the corrosion activity of steel reinforced concrete structures, ASTM STP 1276, Materials and Corrosion, vol. 48. ASTM, West Conshohockem (1997). DOI <https://doi.org/10.1002/maco.19970481109>
13. Knoll, M.D.: A petrophysical basis for ground-penetrating radar and very early time electromagnetics: electrical properties of sand-clay mixtures. Thesis, University of British Columbia (2005)
14. Lai, W.L., Kind, T., Wiggenhauser, H.: A study of concrete hydration and dielectric relaxation mechanism using ground penetrating radar and short-time fourier transform. EURASIP Journal on Advances in Signal Processing 2010(1), 317216 (2010). DOI <https://doi.org/10.1155/2010/317216>
15. Lai, W.L., Kind, T., Wiggenhauser, H.: Frequency-dependent dispersion of high-frequency ground penetrating radar wave in concrete. NDT & E International 44(3), 267{273 (2011). DOI <https://doi.org/10.1016/j.ndteint.2010.12.004>
16. Lai, W.L.W., Kind, T., Kruschwitz, S., Wöstmann, J., Wiggenhauser, H.: Spectral absorption of spatial and temporal ground penetrating radar signals by water in construction materials. NDT & E International 67, 55{63 (2014). DOI <https://doi.org/10.1016/j.ndteint.2014.06.009>
17. Narayanan, R.M., Hudson, S.G., Kumke, C.J.: Detection of rebar corrosion in bridge decks using statistical variance of radar reected pulses. In: Proceedings of the Seventh International Conference on Ground-Penetrating Radar, vol. 98, pp. 27{30 (1998)
18. Orazem, M.E., Tribollet, B.: Electrochemical impedance spectroscopy, second edn. Hoboken, New Jersey: John Wiley & Sons, Inc. (2017)
19. Persico, R.: Introduction to ground penetrating radar: inverse scattering and data processing. Piscataway, NJ : IEEE Press (2014)
20. Poley, J., Nooteboom, J., De Waal, P.: Use of VHF Dielectric measurements for borehole formation analysis, vol. 19. Society of Petrophysicists and Well-Log Analysts (1978)
21. Reynolds, J.M.: An introduction to applied and environmental geophysics. John Wiley, Chichester, New York (1997)
22. Rhim, H.C., Buyukozturk, O.: Electromagnetic properties of concrete at microwave frequency range. ACI Materials Journal 95(3) (1998)
23. Shang, J., Umana, J.: Dielectric constant and relaxation time of asphalt pavement materials. Journal of Infrastructure Systems 5(4), 135{142 (1999). DOI [https://doi.org/10.1061/\(ASCE\)1076-0342\(1999\)5:4\(135\)](https://doi.org/10.1061/(ASCE)1076-0342(1999)5:4(135))
24. Soutsos, M., Bungey, J., Millard, S., Shaw, M., Patterson, A.: Dielectric properties of concrete and their inuence on radar testing. NDT & E International (UK) 34(6), 419{ 425 (2001). DOI [https://doi.org/10.1016/S0963-8695\(01\)00009-3](https://doi.org/10.1016/S0963-8695(01)00009-3)

25. Von Hippel, A.: Dielectric materials and applications. London: Artech House (1954). DOI <https://doi.org/10.1149/1.2430014>
26. Warren, C., Antonis, G.: Guidance on GPR modelling (2019). URL <http://docs.gprmax.com/en/latest/gprmodelling.html>
27. Warren, C., Antonis, G., Giannakis, I.: gprmax: Open source software to simulate electromagnetic wave propagation for ground penetrating radar. Computer Physics Communications 209(C), 163{170 (2016). DOI <https://doi.org/10.1016/j.cpc.2016.08.020>
28. Wong, T.P., Lai, W.L.W., Sham, J.F.C., Poon, C.S.: Hybrid non-destructive evaluation methods for characterizing chloride-induced corrosion in concrete. NDT & E International (2019). DOI <https://doi.org/10.1016/j.ndteint.2019.05.008>
29. Xie, F., Lai, W.W.L., D_erobert, X.: Gpr-based depth measurement of buried objects based on constrained least-square (cls) _tting method of reections. Measurement 168, 108330 (2021). DOI <https://doi.org/10.1016/j.measurement.2020.108330>